Effects of layered liquefiable deposits on the seismic response of an underground structure

Renren Chen[a], Mahdi Taiebat[b], Rui Wang[a,*], Jian-Min Zhang[a]

[a] *Department of Hydraulic Engineering, State Key Laboratory of Hydroscience and Engineering, Tsinghua University, Beijing, China*
[b] *Department of Civil Engineering, University of British Columbia, Vancouver, BC, Canada*

A B S T R A C T

Soil liquefaction poses significant threat to underground structures in seismically active areas. This paper present a detailed numerical investigation on the seismic response of underground structures in horizontally layered liquefiable grounds. A comprehensive plasticity model for large post-liquefaction shear deformation of sand is used for modelling the liquefiable soil layers. A technique of combining beam elements with quadrilateral elements is employed to simulate the response of reinforced concrete structure. Shallow buried underground structures in three typical soil profiles, including a layered liquefiable ground, a homogeneous liquefiable ground, and a homogeneous non-liquefiable ground, are analyzed under seven scaled ground motions, amounting to a total of 21 dynamic calculations. The numerical results show that the existence of a liquefiable layer passing through an underground structure can have detrimental effects on the seismic response of the structure, compared to underground structures embedded either in homogeneous liquefiable and or non-liquefiable ground, causing the structure to suffer larger deformation, bending moment, and shear force. The soil-structure interaction and inertia effects are analyzed to provide explanation for the seismic response of the underground structures.

1. Introduction

Increasing number of underground structures are under construction in China in seismically active areas with liquefiable soil, e.g., Xuzhou and Nanjing. Severe underground structure damage in liquefiable ground has been reported in the past major earthquakes, including the 1995 Kobe earthquake [1,2] and the 2011 Tohoku earthquake [3–5], suggesting that underground structures in liquefiable ground may be vulnerable to seismic damage.

Existing research on underground structures in liquefiable ground have mostly been conducted in homogeneous soil profiles, which have provided important insights into the influence of soil liquefaction on the seismic response of underground structures. Some physical model tests have been carried out, most of which with focus on upheaval caused by soil liquefaction rather than the deformation and internal forces of underground structures during shaking [6–15]. Chen et al. [16] suggested through shaking table tests that internal columns are easily damaged under strong horizontal forces on sidewalls. Zhuang et al. [17] found that lateral spreading led to large residual internal forces in underground structures. Several centrifuge model test studies on underground structures in liquefiable ground indicated that the base

of pillars and the intersections of sidewalls and floors are prone to failure during shaking [18]. Numerical studies on the seismic response of underground structures in homogeneous liquefiable soil have also been carried out using elastic or elasto-plastic structure models, along with soil models of various complexity [19–26]. However, in practice, few underground structures are built in homogeneous liquefiable soil. Instead, layered soil profiles with liquefiable layers passing through parts of underground structures are much more widely encountered. For example, Subway Line 1 of Nanjing in China, from Xufuxiang Station to Nanjing Station passes through a non-uniform liquefiable area (Fig. 1, [27]). Hashash et al. [28,29] suggested that underground structures partially or entirely embedded in liquefiable soil require additional evaluation. Hence, an important question must be answered: are underground structures in layered liquefiable ground more or less susceptible to seismic damage compared with those in homogenous non-liquefiable and liquefiable ground, and why?

Recent developments in numerical simulation methods provide a feasible means to investigate this problem. To appropriately model liquefiable soil and structure interaction during seismic events numerically, the plasticity of underground structures should be considered, and as importantly, constitutive models that reflect the liquefaction
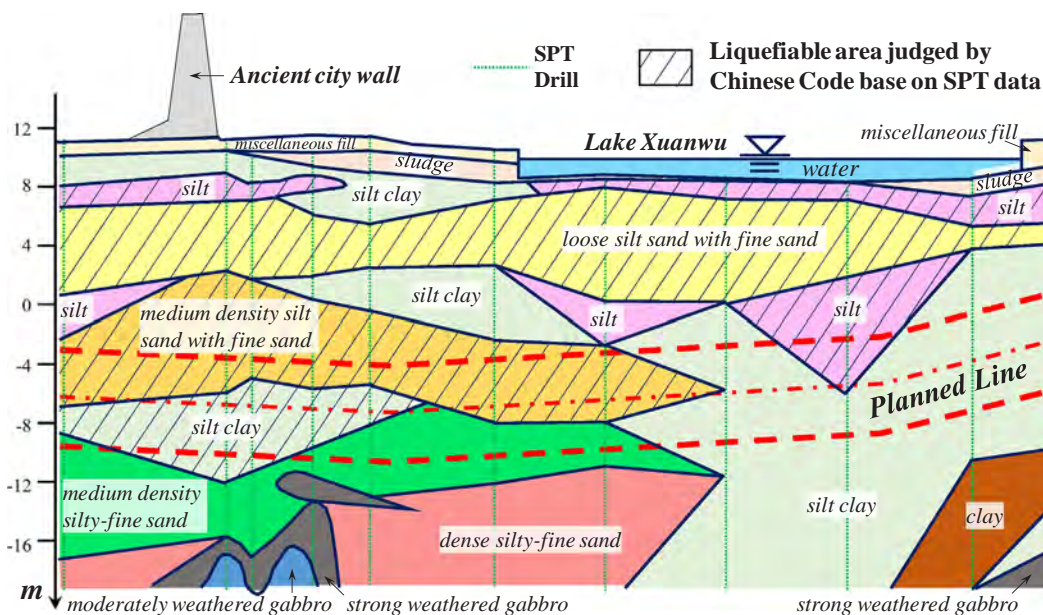

Fig. 1. Geological section for Subway Line 1 from Xufuxiang Station to Nanjing Station in Nanjing, China (based on Wang and Yan, [27]).
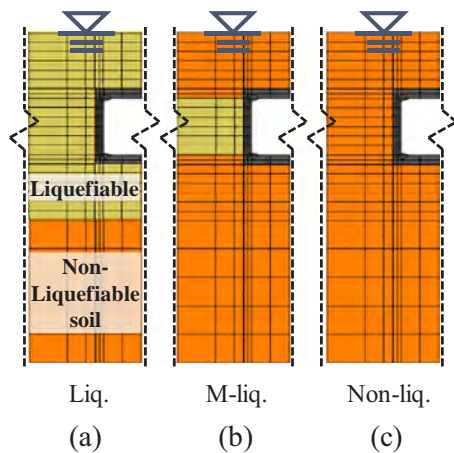

Fig. 2. Idealized soil layering conditions with respect to the location of the underground structure.

behavior of soil along with solid-fluid coupled formulations should be adopted. Several constitutive models have enhanced the description of cyclic behavior of sand [30–35], and can be useful in conducting dynamic analysis on underground structures in liquefiable ground.

This paper investigates the seismic response of an underground structure embedded in various horizontally layered grounds with a liquefiable sublayer, using high fidelity numerical modelling methods. Section 2 presents the numerical analysis details, including analysis conditions and procedure, structure and soil models, and input motions. In Section 3, analysis results for seismic response of the base case underground structure in a layered liquefiable ground is presented. The influence of layered liquefiable ground is analyzed in Section 4, through comparison of the structure response, soil deformation, and soil-structure interaction of the underground structure in layered and homogeneous soil profile conditions.

2. Numerical analysis setup

2.1. Analysis conditions and procedure

For this study, a hypothetical underground structure, representing a subway station at 6–14 m depth, is considered in a 35 m thick saturated soil stratum. Three typical soil profile conditions are analyzed, including a 20-meter liquefiable layer overlying a non-liquefiable layer, a 6-meter liquefiable layer at 7–13 m depth in between two non-liquefiable layers, and a homogeneous non-liquefiable soil. The soil layering and the location of the underground structure for each one of these three profiles are illustrated in Fig. 2. The underground structure is fully embedded in the liquefiable layer in the first condition (labelled "Liq" in Fig. 2(a)). The liquefiable layer in the second condition passes through the underground structure, with the sidewalls in contact with the liquefiable layer, and the top and bottom slabs in contact with non-liquefiable soil (labelled "M-liq" in Fig. 2(b)). The case of underground structure in homogeneous non-liquefiable soil is analyzed under the third condition as a benchmark for comparison (labelled as "Non-liq" in Fig. 2(c)).

Plane strain analysis is conducted using the OpenSees framework [36]. Based on the geological layering in Nanjing [37], the high shear wave velocity bedrock usually starts at depth of 20–40 m. Hence, for simplification a rigid base boundary condition is used for the application of the earthquake input motion at the base of the model [38]. The bottom boundary of the model is constrained to follow the input motion, and is set as an impermeable boundary. Tied displacement degrees of freedom are used at the two lateral boundaries to simulate the free-field motion. The water level is assumed to be at the ground surface, with a free drainage boundary condition.

To set up the initial stress state, gravity field is applied in the model followed by excavation of the underground space and placement of the underground structure, following the procedures proposed by Wang et al. [39]. Dynamic analysis is then carried out, followed by another 100 s of calculation after the earthquake motion to allow for dissipation of excess pore pressures. Details of the numerical model, including the elements, constitutive models, and input motions, are presented in the following sections.

2.2. Structure model

The hypothetical underground structure represents a typical 8 m height one-story and two-span subway station based on the practical design, with the top slab 6 m below ground surface. 0.5 m × 0.5 m square cross section pillars with 3 m spacing are in the middle, which would be modelled as equivalent wall in the next content but still called
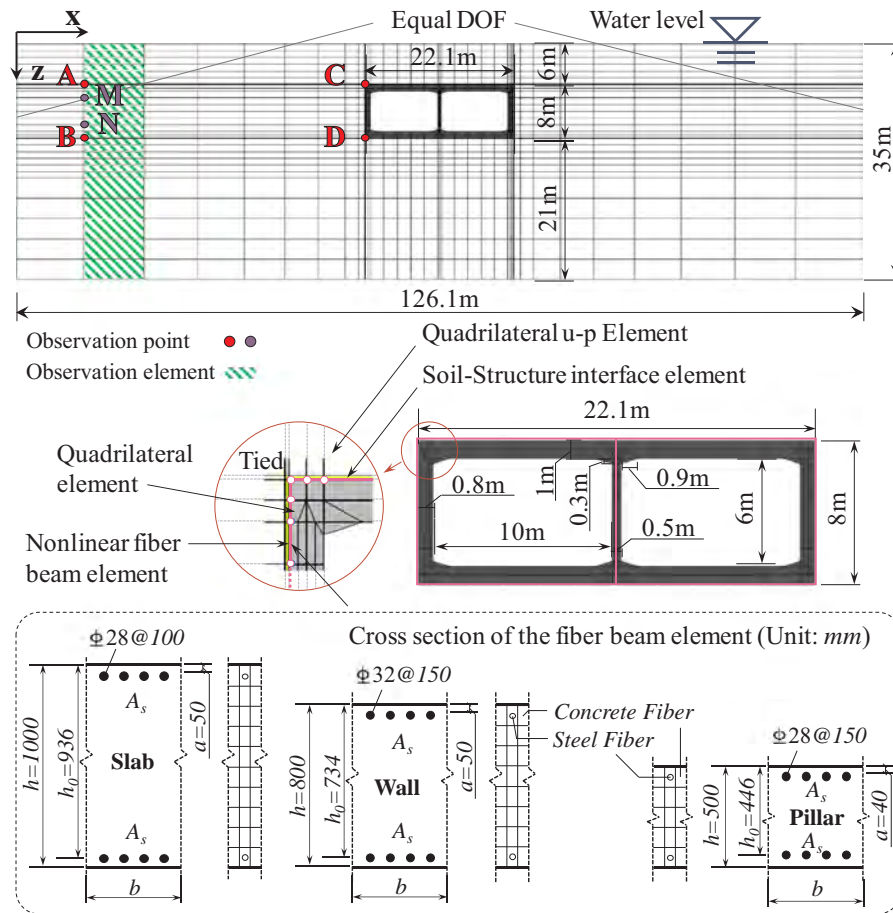
Fig. 3. Geometry of the numerical model; spatial discretizations; locations of the control points A-D, M, and N; and structural details of the underground reinforced concrete structure.

pillar for short. Details on the geometry of the numerical model, spatial discretizations, locations of the control points A-D, M, and N, and structural details of the underground reinforced concrete structure are shown in Fig. 3.

As 2D analysis is carried out in this study, an equivalent modulus is used for the pillars, which is the actual modulus multiplied by the ratio of pillar thickness and pillars center-to-center distance (0.5 m/3.5 m). The bending moment capacity of the structure is decided by the sectional reinforcement, geometrical size, and material strength [40]. As the walls are continuous in the longitude direction, their strength indices are presented as per meter for the wall, while those for the central pillar are presented in per pillar terms. The bending moment capacities are 1091 kN m/m and 217 kN m for the walls and central pillar, respectively. The corresponding shear capacities are 2062 kN/m and 88 kN.

The underground structure is modelled using combined elements that consist of both quadrilateral elements and nonlinear fiber beam elements. On one hand, the quadrilateral element can provide a volumetric representation of the structure, but cannot give a good representation of the properties of reinforced concrete. On the other hand, the nonlinear fiber beam element excels at representing the cross-section properties of reinforced concrete, while not being able to reflect the volume of the structure. Therefore, by tying the beam element, which provides the stiffness of the structure, to the quadrilateral element, which provides the geometry of the structure, the combined element takes advantage of the strengths of both elements. To validate this combined element approach, a 6-meter elastic cantilever ($E = 32.5$ GPa) with 0.5 m × 0.5 m square section is modelled (Fig. 4(a)), with nonlinear fiber beam elements tied to quadrilateral

elements. The stiffness of the beam elements is the same as the cantilever, while the modulus of the quadrilateral elements is set to 0.0001 times that of the cantilever, so that the stiffness of the cantilever is provided almost entirely by the beam elements. The bending moment, shear force, and deflection calculated using the proposed combined element show excellent agreement with the Euler beam theoretical solution. In addition, a 6-meter elastic-plastic reinforced concrete cantilever with 0.8 m × 1.0 m cross-section is modelled (Fig. 4(b)), subjected to lateral displacement loading on the top. In the fiber beam elements used in this study, steel reinforcement is modelled using the Giuffre-Menegotto-Pinto model (Steel02), which can simulate the Bauschinger effect, and concrete is modelled using the Kent-Scott-Park model (Concrete01), which ignores the tensile strength in accordance with the practical design for reinforced concrete structures. Linear elastic material is used in the quadrilateral elements with 0.0001 times that of the actual modulus of the structure. The bending moment at the bottom of the cantilever is plotted against the lateral load in Fig. 4(b), which shows that the combined elements can accurately reflect the designed moment capacity of the reinforced concrete cross-section.

2.3. Soil models

A *u-p* formulation [41] quadrilateral FourNodeQuadUP solid-fluid coupled element [42] based on Biot's theory for porous medium is adopted for the soil domain in this study. The liquefiable soil is modelled using the unified plasticity model for large post-liquefaction shear deformation of sand (CycLiqCPSP) developed by Wang et al. [35] and Wang [43]. The constitutive model works within the bounding surface plasticity framework [44]. It incorporates critical state soil mechanics
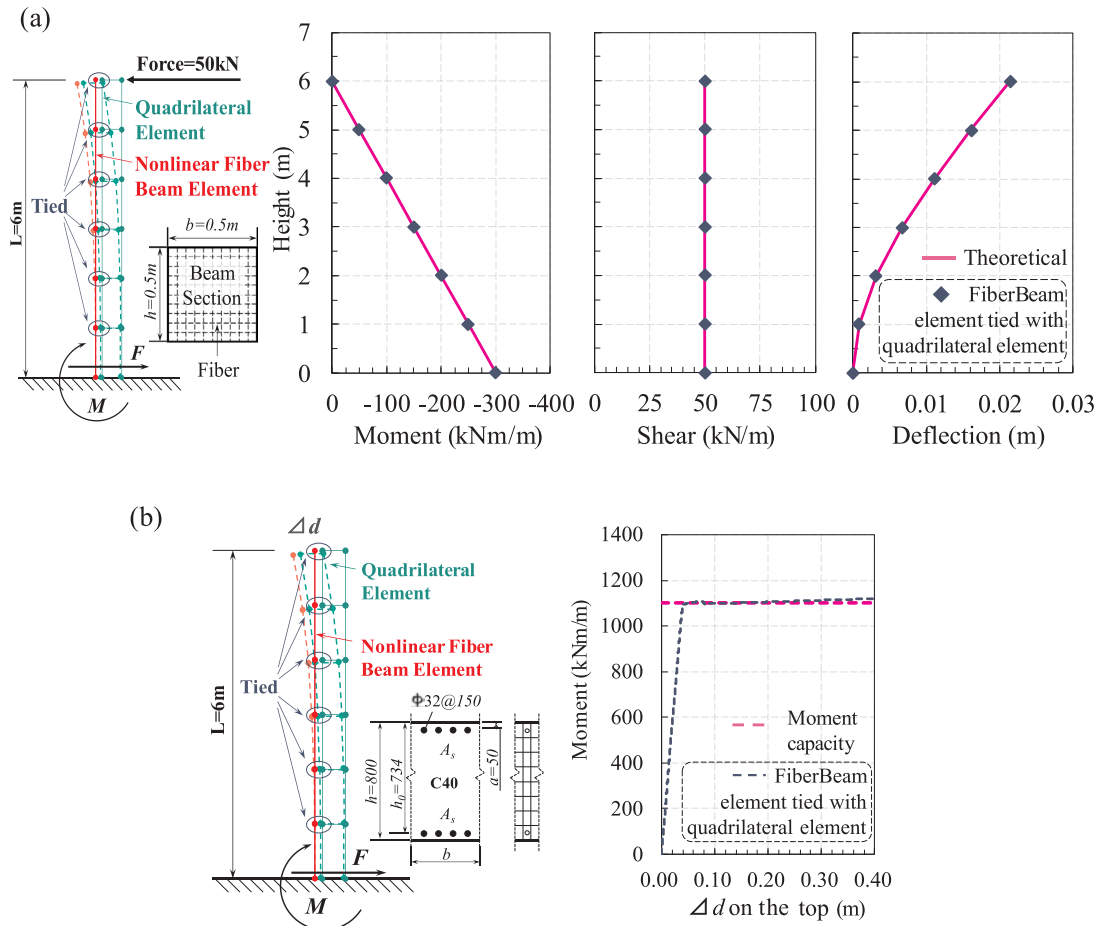
Fig. 4. Validation of the proposed combined structural element in (a) calculating the bending moment, shear force, deflection, and (b) capturing the bending moment capacity of a cantilever beam under lateral loading.

to achieve a unified description of saturated sand of different states from pre- to post-liquefaction stages, through appropriate formulations for the dilatancy of sand. The model has been validated against a wide range of monotonic/cyclic drained/undrained laboratory tests and centrifuge model tests, and has been successfully applied to several soil-structure interaction studies [23,39,45]. The model parameters used in this study are selected based on typical values for liquefiable sand, as listed in Table 1, including elastic modulus constants (G_0, κ), plastic modulus parameter (h), critical state parameters (M, λ_c, e_0, ξ), state parameter constants (n^p, n^d), reversible dilatancy parameters ($d_{re,1}$ $d_{re,2}$) and irreversible dilatancy parameters (d_{ir}, α, $\gamma_{d,r}$). Details of the model can be found in Wang et al. [35]. Typical element level cyclic behavior of the liquefiable soil with the proposed model parameters, under undrained cyclic torsional loading, with initial mean effective stress of 100kPa and shear stress amplitude of 25kPa, are shown in Fig. 5. The result illustrates the simulative capability of the model under undrained cyclic loading in producing both the reduction of effective stress in the pre-liquefaction stage and the accumulation of shear strains in each cycle after the material reaches initial liquefaction.

Non-liquefiable soil is modelled using elastic perfect-plastic Mohr-Coulomb model for simplification. The parameters for non-liquefiable soil are obtained based on geological exploration results in Nanjing, including elastic modulus (E), Poisson's ratio (ν), cohesive stress (c) and frictional angle (φ). Soil-structure interface is modelled using the Clough-Duncan interface model [46], with material parameters obtained from Wang et al. [39]. Similar to a number of other liquefaction numerical studies [47–49], the Rayleigh damping adopted in the present analysis, combines a fraction α of the mass matrix with a fraction β of the stiffness matrix. These coefficients can be calculated by selecting

an initial damping ratio and concerned frequency range, which are taken as 5% aiming at around 0.5 s period for the present system.

2.4. Input motions

Following the recommendation of the National Earthquake Hazards Reduction Program (NEHRP) [50] for selecting and scaling earthquake ground motions for performing response-history analyses, and the approach of Taiebat et al. [51] in a similar study on the seismic response of basement walls, seven ground motions were selected using the Pacific Earthquake Engineering Research Center (PEER) ground motion database [52], as explained below. Selection of the candidate ground motions was done for linear scaled matching to the Uniform Hazard Spectra (UHS) proposed by the Chinese Code for Seismic Design of Buildings (CCSDB) [53] for Nanjing. The geological exploration data in Nanjing Subway Line 1 shows that the ground falls into site class II, with average shear wave velocity from 150 m/s to 250 m/s in 3–50 m depth, and 250–350 m/s in deeper than 5 m depth. Near source events were excluded. The search for appropriate earthquake records was constrained by a range of magnitudes and distances to earthquake sources. More specifically, a moment magnitude range of M_w = 5.9–7.35 is used, and earthquake source distance of smaller than 100 km is considered during selection, owing to the uncertainties about the locations of the active faults in the Nanjing area.

The selected ground motions, linearly matched to the UHS, are then baseline corrected with a linear function and filtered with a bandpass Butterworth filter with cut-off frequencies of 0.1 and 25 Hz, using the computer program SeismoSignal [54]. The end result of this process is a suite of ground motions, G1–G7, as presented in Table 2 and Fig. 6, that

Table 1

Constitutive model parameters adopted for the soil layers, structural elements, and interface layers (a), and the corresponding density and permeabily values where applicable (b).

(a)

CycLiqCPSP	Sand	Mohr Coulomb	Non-liquefiable soil	
G_0	100	E	147 MPa	
κ	0.006	υ	0.473	
h	0.6	c	30kPa	
M	1.25	φ	26°	
$d_{re,1}$	0.02			
$d_{re,2}$	40	Elastic	Slabs &Walls[a](C40)	Pillar[a](C50)
d_{ir}	0.5	E	32.5 GPa	34.5 GPa
α	90	ν	0.2	0.2
$\gamma_{d,r}$	0.05			
n^p	1.1	Giuffre-Menegotto-		
n^d	8	Pinto steel		
λ_c	0.019	f_y	300 MPa	300 MPa
e_0	0.837	E_0	200Gpa	200Gpa
e_{in}	0.717	b	0.00001	0.00001
ξ	0.7	Kent-Scott-		
Clough Duncan	Interface	Park concrete		
G_0	150	f_{pc}	19.1 MPa	23.1 MPa
n	0.52	ε_{c0}	0.002	0.002
φ	30°	f_{pcu}	9.55 MPa	11.55 MPa
R_f	0.65	ε_{c1}	0.0033	0.0033

(b)

	Density	Permeability[b]
Liquefiable soil	1.961 g/cm³	0.00023 m/s
Non-liquefiable soil	2.05 g/cm³	0.000076 m/s
structure	2.43 g/cm³	0

  [a] Modulus in quadrilateral element for walls and pillar is reduced to 0.0001 times. C40 and C50 represent grade of concrete.

  [b] Permeability in the interface element is assumed to be the same as that of the contact soil.

correspond to the 2% in 50 year hazard level specified for Nanjing. These seven ground motions were used in the dynamic analyses of this study, as discussed in the next sections.

3. Typical results

To illustrate the typical response of the underground structure in a layered liquefiable ground, the analysis results for the M-liq condition under ground motion G1 are presented in this section. The basic response of the far-field soil at points M and N and the underground structure at base points of the left and right walls and central pillar are presented in Figs. 7–9.

The far-field soil acceleration at different depths is shown in Fig. 7(a), which exhibits significant attenuation compared with the input motion. One of the important characteristics of liquefiable ground is the accumulation of the excess pore pressure and the reduction of the

Table 2

List of selected ground motions.

No.	Scale factor	Earthquake name	Year	Station name	Magnitude	V_{s30}(m/s)
G1	8.59	Friuli_Italy-02	1976	"Codroipo"	5.91	249
G2	2.08	Tabas_Iran	1978	"Boshrooyeh"	7.35	325
G3	0.91	Imperial Valley-06	1979	"EC County Center FF"	6.53	192
G4	1.33	Victoria_Mexico	1980	"Chihuahua"	6.33	242
G5	3.94	Trinidad	1980	"Rio Dell Overpass - FF"	7.2	312
G6	0.87	Irpinia_Italy-01	1980	"Sturno (STN)"	6.9	382
G7	1.07	San Fernando	1971	"LA - Hollywood Stor FF"	6.61	316

effective stress of soil under earthquake excitation. As shown in Fig. 7(b), the excess pore pressure ratio (EPPR) at − 8 m reaches 1.0 towards the end of the input motion, indicating liquefaction in the soil layer. Although the soil below − 12 m does not fully liquefy, significant increase in excess pore pressure is observed. The time histories of the soil horizontal displacements are presented in Fig. 7(c), which show strong oscillations during the input motion and very little residual deformation. In addition, typical stress-strain relationship and stress paths at different depth are presented in Fig. 8, showing that zero effective stress is reached at − 8 m depth, while the vertical effective stress decreases but does not reach zero at − 12 m.

Fig. 9 presents the time histories of shear force and bending moment of the structure, at the bottom of the left wall, pillar, and right wall, respectively. The internal forces in walls are significantly greater than those in the central pillar; this is consistent with the general expectation that the design capacity for walls in practice should generally be greater than that of the pillar. During the G1 motion in the M-liq condition, the moment at the bottom of the left wall and central pillar reaches the design moment capacity (1091 kN m/m and 217 kN m) at 13.5 s, while the moment at the bottom of the right wall reaches the design moment capacity (1091 kN m/m) at 4.2 s.

4. Influence of layered liquefiable ground

4.1. Structure response

Drift ratio, bending moments, and shear forces within the underground structures may be considered as measures of their seismic performance. The drift ratio is the absolute differential lateral displacement of the top and bottom of the underground structure normalized by the height of the structure. Based on Eurocode 8 (2005) [55], ASCE 7 (2005) [56] and CCSDB [53], the drift ratio should be restricted to smaller than 1.0%, 0.7% and 0.4%, respectively, in which the minimum one is adopted as limitation value, while the bending moment and shear
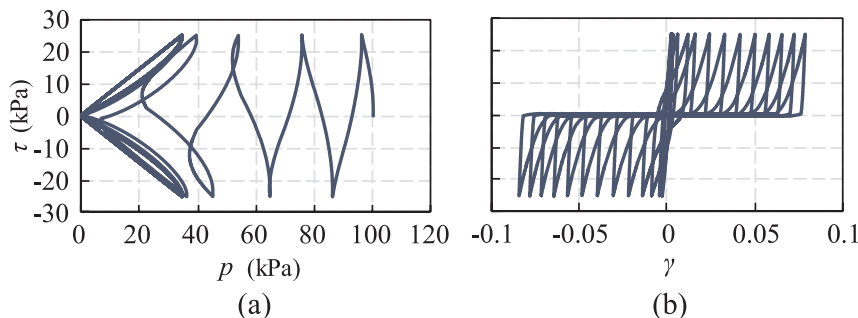

Fig. 5. Typical undrained cyclic torsional shear response of the liquefiable sand using the model parameters selected in this study.
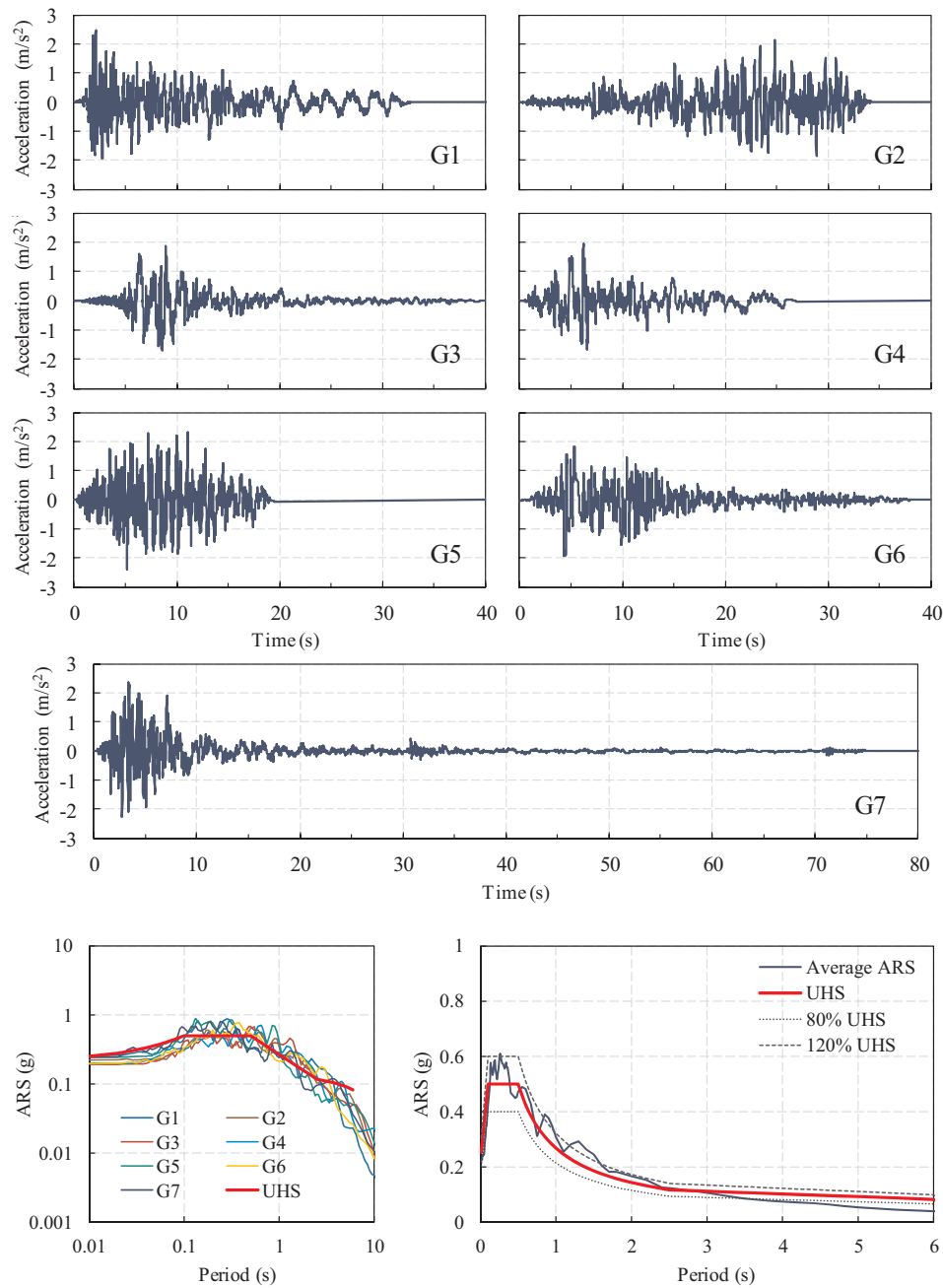
Fig. 6. Acceleration time histories and response spectra (5% damping) of the selected ground motions, linearly matched to the UHS of Nanjing in the period range of 0.02–6.0 s.

force should be within their respective design capacity values.

Under each of the ground motions G1-G7, the drift ratio of the underground structure varies within its maximum value. An "average range of drift ratio" for ground motions G1-G7 can be introduced such that it represents the range within the average maximum values. Fig. 10 shows average range of drift ratio for motions G1-G7 in each of the three soil profile conditions. The average maximum drift ratio in the M-liq condition is 120% greater than that in the Non-liq condition, and is 50% greater than that in the Liq condition. In this study, the drift ratio values in all of three conditions are well smaller than the threshold value from the adopted performance criterion.

Fig. 11 shows the distribution of maximum moments, averaged over the seven input motions, along the left wall, central pillar, and right wall, respectively, in the Liq, M-liq, and Non-liq conditions. The bending moment capacities of the walls and central pillar sections are

also presented for reference. The maximum bending moment values occur at the two ends of the walls and the pillar. The average maximum bending moment in both ends of the walls and the pillar in the M-liq condition reach the moment capacities, which could lead to damage of the structure. In the Non-liq condition, the average maximum bending moments remain well within the moment capacities. In the Liq condition, the maximum bending moments at the top of the side walls and the pillar are in safe range, but the bending moment at the bottom of the side walls are close to the moment capacity, with safety factors of only 1.02 and 1.06 for the left and right walls, respectively. The results clearly show more critical conditions for the M-Liq condition of soil layering.

The distribution of maximum shear forces averaged over the seven input motions are plotted in Fig. 12 along the left wall, central pillar, and right wall, respectively, under the three different soil conditions.
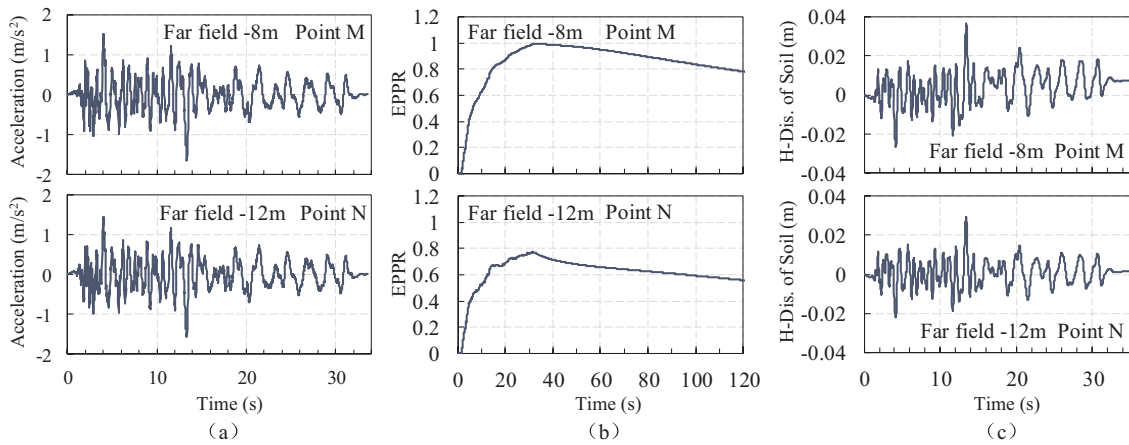
Fig. 7. Typical soil response in the of far-field at two depths within the liquefiable layer in the M-liq condition during G1 motion: time histories of (a) accelerations, (b) excess pore water pressure ratios, (c) lateral displacements.
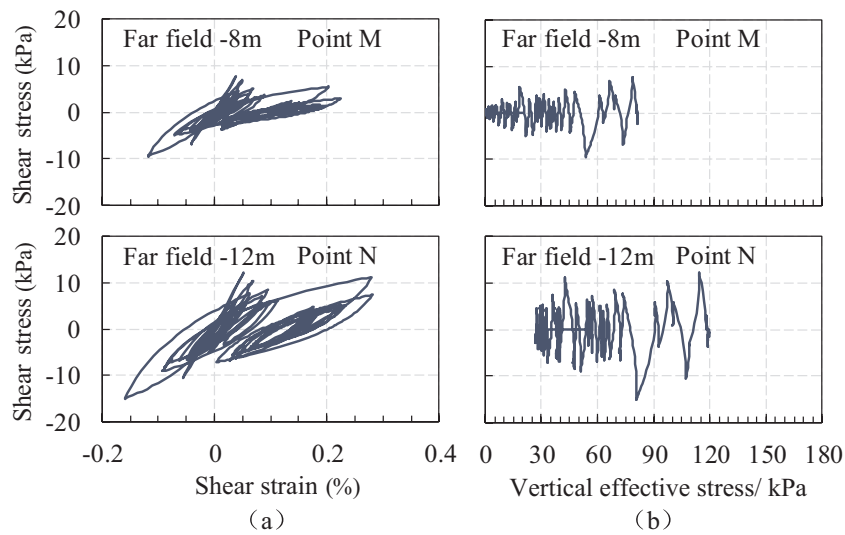

Fig. 8. Typical soil response in the of far-field at two depths within the liquefiable layer in the M-liq condition during G1 motion: (a) stress-strain loops, and (b) effective stress paths.
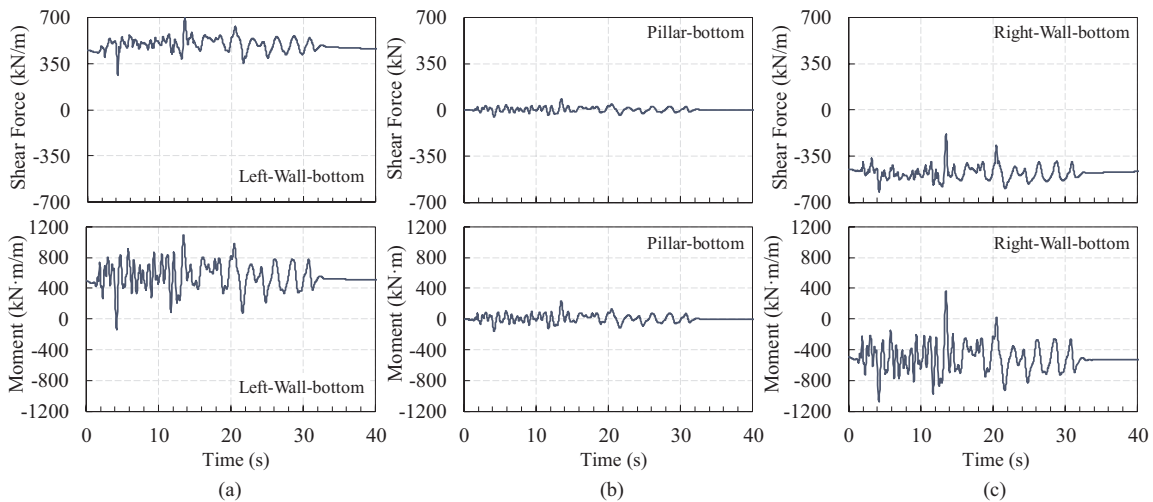

Fig. 9. Typical response of the underground structure in the M-liq condition during G1 motion: time histories of the shear forces and bending moments at the bottom of the (a) left wall, (b) pillar, and (c) right wall.
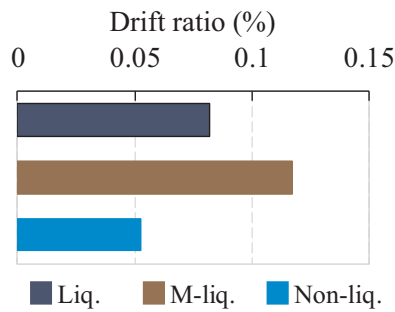
Fig. 10. Range of drift ratio averaged over ground motions G1-G7 in each of the three soil profile conditions.

Fig. 13. Range of differential horizontal displacement of far-field soil within the depth of the structure averaged over ground motions G1-G7 in each of the three soil profile conditions.

The shear capacities of the walls and central pillar sections are also presented for reference. The average maximum shear force distribution is concave with the largest shear force occurring at the top and bottom of the walls, and is well within the shear capacity under all conditions. In the central pillar, the envelope of average maximum shear force increases slightly from top to bottom along the height of the structure. In the M-liq condition, the maximum shear force at the pillar bottom is close to the shear capacity, and is highest among the three conditions.

Through comparison of structure deformation and internal forces of three different soil profile conditions, the M-liq condition with layered liquefiable soil experiences the highest drift ratio, bending moments, and shear forces. This suggests that under the same input motion, layered liquefiable soil profile could induce higher demand on the underground structure, and is an unfavourable condition compared with the case of underground structure embedded in homogeneous liquefiable soil, and of course compared with the case of underground structure embedded in homogeneous non-liquefiable soil. Therefore,
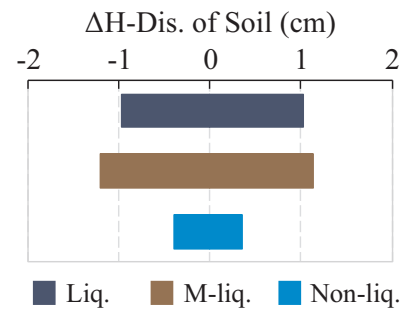
more attention should be paid to the seismic safety of underground structures when they are embedded in layered liquefiable soil profile, which is widely observed in actual practice. In order to understand the mechanisms behind the influence of layered liquefiable soil profile on the seismic response of underground structures, further analysis of ground deformation and soil-structure interaction is conducted in the following sections.

4.2. Ground deformation

Ground deformation significantly influences the response of underground structures. The ranges of differential horizontal displacement ΔH between the elevations of the top and bottom of the underground structure in the far field (point A and B, Fig. 3) averaged over the seven input motions in each of the three soil profile conditions are presented in Fig. 13. The maximum ΔH in the M-liq condition is 20%
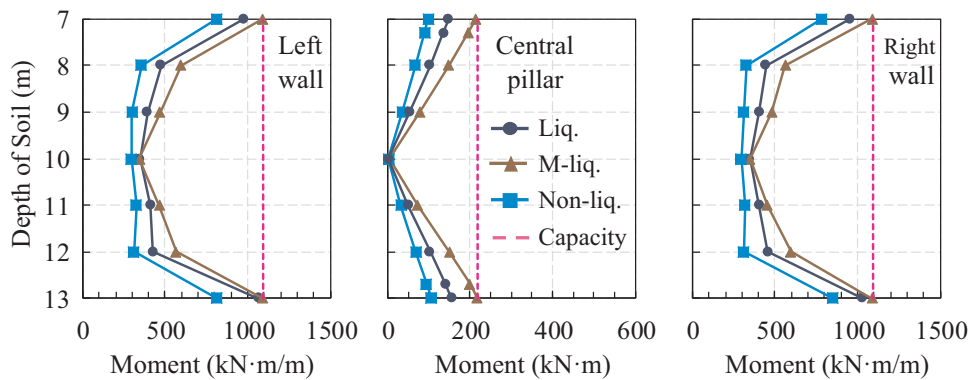

Fig. 11. Distribution of maximum absolute moment, averaged over ground motions G1-G7, along the left wall, central pillar and right wall in each of the three soil profile conditions. The bending moment capacities of the walls and central pillar sections are also presented for reference.
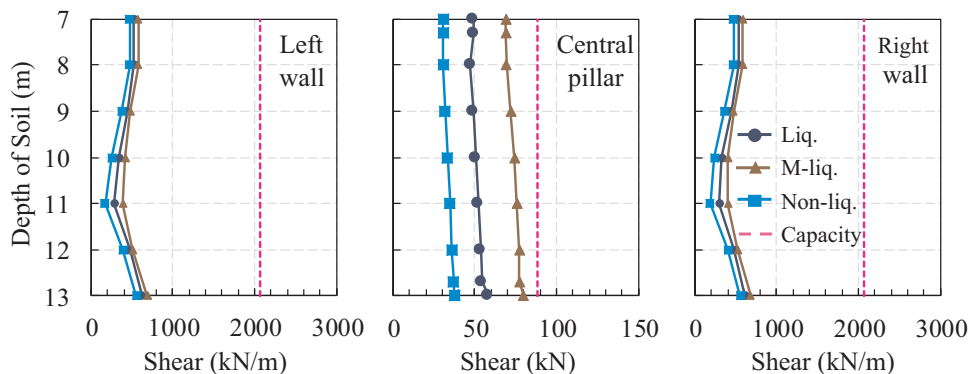

Fig. 12. Distribution of maximum absolute shear force, averaged over ground motions G1-G7, along the left wall, central pillar and right wall in each of the three soil profile conditions. The shear capacities of the walls and central pillar sections are also presented for reference.
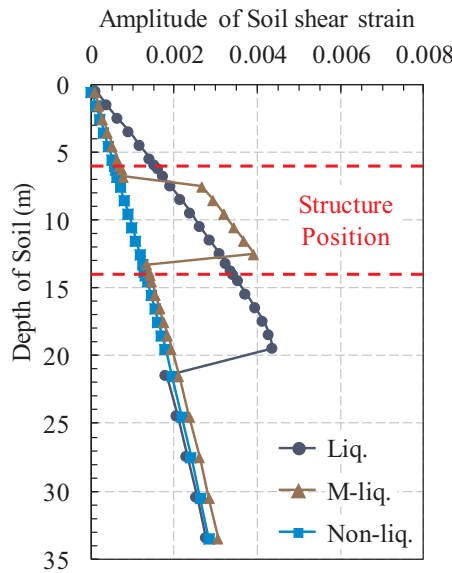
Fig. 14. Profile of the shear strain amplitude of far-field soil averaged over ground motions G1-G7 in each of the three soil profile conditions.

greater than that in the Liq condition. The maximum ΔH in the Non-liq condition is much smaller than that in the other two conditions with liquefiable soil.

Fig. 14 shows the amplitude of shear strain in the far field soil from

ground surface to the base of the model averaged over the seven ground motions, obtained from the marked observation elements in Fig. 3. A striking observation from this figure is the significant increase of shear strain in the liquefiable layers compared with the non-liquefiable layers in the M-liq and Liq conditions. The shear strain in the liquefiable layer in the M-liq condition is even greater than that in the Liq condition at the same depth. The amplitude of shear strain in the non-liquefiable layers is similar in all three soil profile conditions. The shear strain results are in agreement with the observed far-field differential horizontal displacement at the underground structure depth, the relatively large shear strain within the liquefiable layer leads to large differential horizontal displacement in the M-liq and Liq soil profile conditions, which can be expected to significantly affect the seismic response of the underground structure.

4.3. Soil-structure interaction: kinematic and inertial

The deformation of soil during a seismic event induces external forces on the underground structure. The inertial forces of the structure also contribute to the soil-structure interaction. The effects of soil-structure interaction are evaluated in this section through analysis of the horizontal normal forces on the walls and shear forces on the top and bottom slabs. The influence of inertia forces on the structure is also analyzed.

Fig. 15 shows the initial normal forces and the maximum dynamic normal force increments on the walls averaged over the seven input motions in each of the three soil profile conditions. The normal force comprises of effective soil pressure and water pressure, which is calculated by integrating the horizontal normal effective stress from the
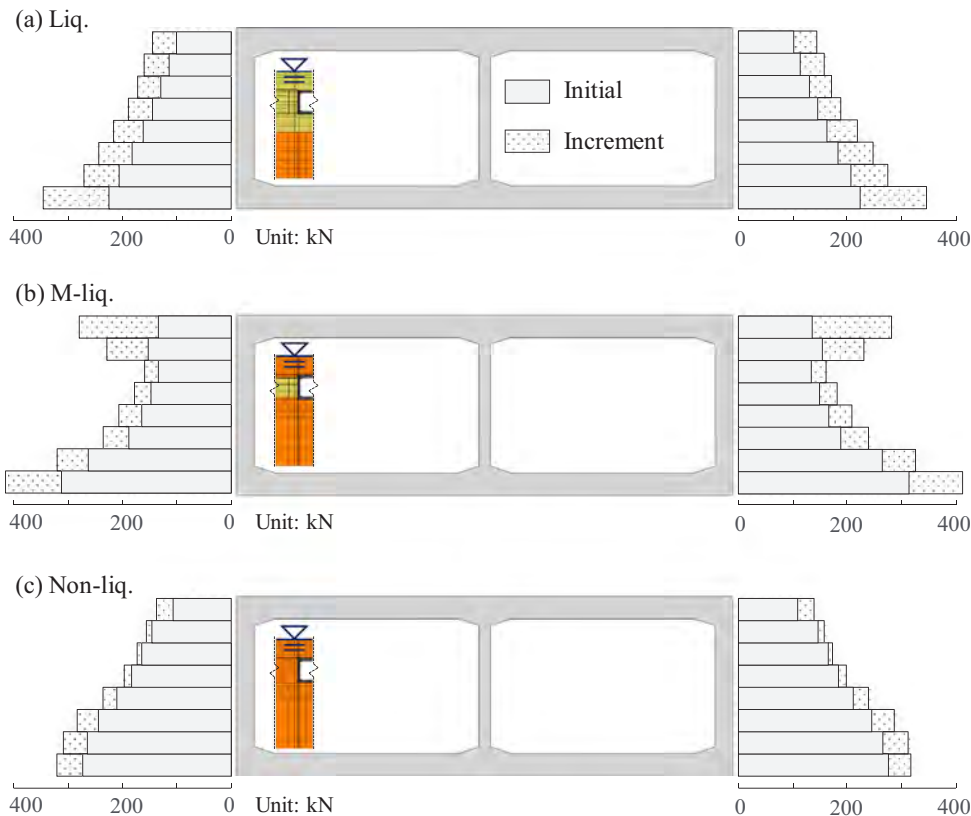

Fig. 15. Initial normal forces and the maximum dynamic normal force increments on the walls averaged over ground motions G1-G7 in the three soil profile conditions.
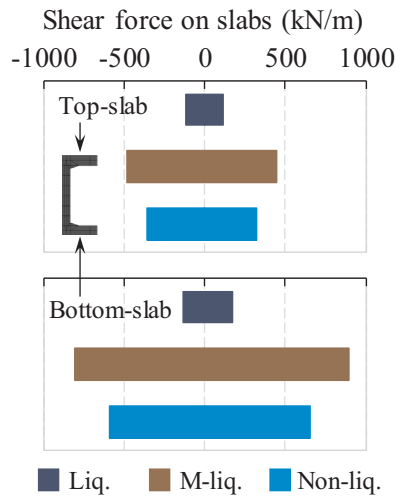
Shear force on slabs (kN/m)

Fig. 16. Range of shear force on top and bottom slabs averaged over ground motions G1-G7 in each of the three soil profile conditions.

soil and pore pressure along the height of the walls. The dynamic normal force increments in the Liq and M-liq conditions are greater than those in the Non-liq condition. The incremental normal force at the top of the sidewalls in the M-liq condition is significantly greater than that in the Liq and Non-liq conditions, which could lead to stronger shear of the underground structure.

The dynamic incremental horizontal normal force on the walls is not the sole cause of the deformation and internal forces of underground structures, the shear forces on the top and bottom slabs also play a key role. Fig. 16 shows the range of shear forces on top and bottom slabs of the underground structure averaged over the seven input motions in each of the three soil profile conditions. It is evident that the shear force in the M-liq condition is the greatest, which is 40% greater than the Non-liq condition and as much as five times that of the Liq condition. For further explanation, Fig. 17 shows the variations of the mean shear

strain of interface soil and the corresponding mean shear stress on the slabs slabs adjacent to the top and bottom slabs for G1 motion in the soil conditions Liq and M-Liq. In the Liq condition, liquefaction takes place under the bottom slab of the structure, which leads to the low stress levels with significant shear strains. In the M-liq condition, since no liquefaction takes place on the slabs, the increase in shear strain of the liquefied layer would increase the shear force on the structure. The significantly greater shear force acting on the top and bottom slabs of the underground structure in the M-liq condition compared with that of the other two conditions provides explanation to why the structure response in the M-liq condition is the most intense of the three conditions.

For the Liq condition, the shear forces on the top and bottom slabs are significantly smaller than those in the Non-liq condition, yet its structure response is more intense than that in the Non-liq condition. This can be explained through analysis of the inertial forces on the underground structure, which is often overlooked. The acceleration distribution in the structure under G1 motion at the time of maximum drift ratio in each condition is plotted in Fig. 18. The structure under all the three conditions reaches its maximum drift ratio, being 0.08%, 0.12%, and 0.05% for the Liq, M-liq, and Non-liq conditions, respectively. At these maximum drift ratios, the differential acceleration between the top and bottom slab are around $0.24 \, \text{m/s}^2$ and $0.35 \, \text{m/s}^2$, respectively, in the Liq and M-liq conditions (Fig. 18(a,b)). However, in the Non-liq condition, although the absolute values of acceleration are greater than those in the other two conditions, the differential value between the top and bottom slabs is much smaller, at around $0.12 \, \text{m/s}^2$ (Fig. 18(c)). This indicates that the loss of constraint from the liquefied soil in the Liq. and M-Liq. conditions can lead to greater differential acceleration in the underground structure compared to that of underground structures in non-liquefied soil, which in turn increases the internal forces and deformation in the structure for the former conditions. Unlike the existing perception that inertial forces are negligible for underground structures, these results suggest that for underground structures in liquefiable ground, inertial forces can also have a strong impact on seismic response.
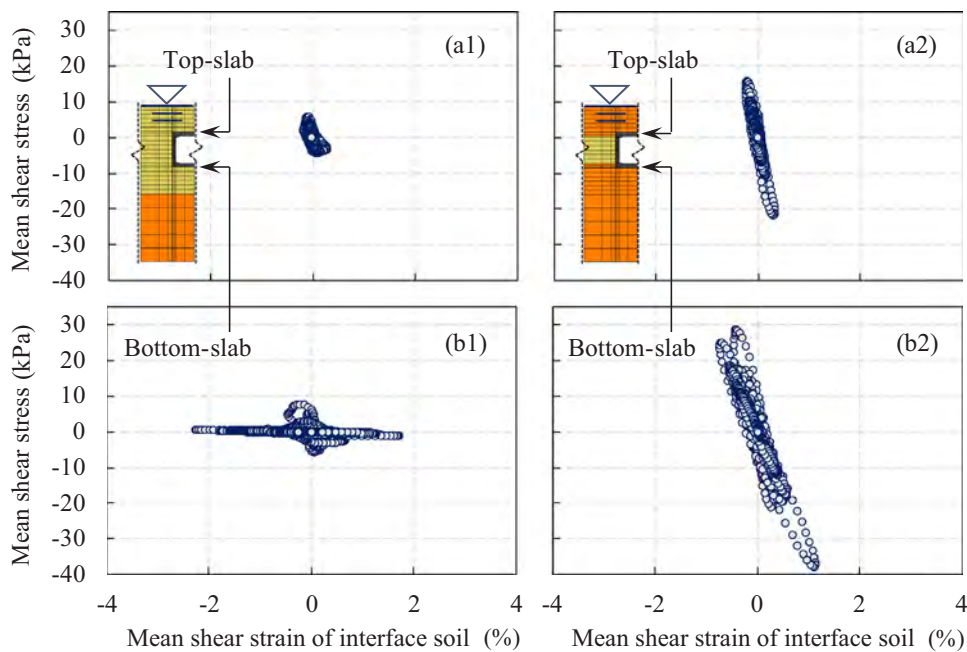

Fig. 17. Variations of the mean shear strain of interface soil and the corresponding mean shear stress on the slabs adjacent to the top and bottom slabs for G1 motion in the soil conditions Liq and M-Liq.
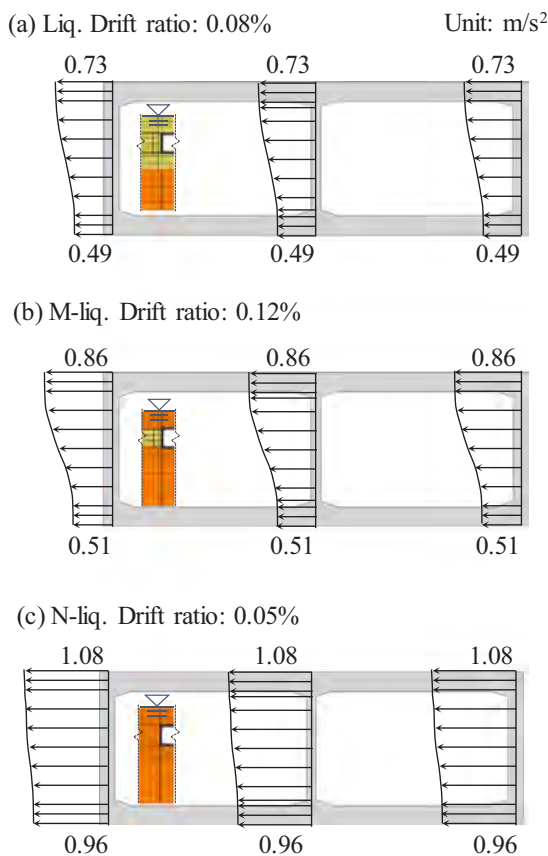
(a) Liq. Drift ratio: 0.08% Unit: m/s²

(b) M-liq. Drift ratio: 0.12%

(c) N-liq. Drift ratio: 0.05%

Fig. 18. Acceleration distribution on the structure at the time of maximum drift ratio for ground motion G1 in each of the three soil profile conditions.

5. Conclusions

Numerical analysis on the seismic response of a one-story and two-span underground structure is conducted in this study for three different soil profile conditions, including a layered liquefiable ground, a homogeneous liquefiable ground, and a homogeneous non-liquefiable ground. PEER database was used to select and scale seven linear matched ground motions to the UHS of a particular site, for the analyses. A comprehensive plasticity model for large post-liquefaction shear deformation of sand was used for the liquefiable soil, and an elastic perfect-plastic Mohr-Coulomb model was used for the non-liquefiable soil. A new combined structure element modelling technique was used to represent both the cross-section properties and the volume of the reinforced concrete, by tying together non-linear fiber beam elements with quadrilateral elements. Drift ratios, bending moments, and shear forces of the underground structure were used to evaluate its dynamic response.

For the shallow buried underground structures, the existence of the liquefiable soil around the structure could cause the structure to be more prone to failure compared with the same structure in non-liquefiable ground. In this study, for the structures in liquefiable ground, the bending moment in several parts of the structure reached or almost reached the moment capacity, and the shear force in the central pillar in the M-liq condition was close to its shear capacity. However, the drift ratio of the structure was well within the limit value, suggesting that the current limitation value requirement for underground structures may need to be reduced.

Layered liquefiable soil has a significant influence on seismic response of underground structures. Compared to the other two conditions, the structure in the M-liq condition suffers the greatest drift ratio, bending moment, and shear force. This is caused by the large shear strain within the liquefiable layer, along with the large shear force that is applied on the top and bottom slabs of the structures by the overlaying and underlying non-liquefiable soil. Therefore, the case of a liquefiable layer passing through the underground structure is actually a more dangerous case compared to cases with idealized homogeneous ground.

The distribution of inertial force in underground structures was found to be important for the seismic response of underground structures in liquefiable ground. In liquefiable ground, the loss of constraint from the liquefied soil can lead to greater differential acceleration in the underground structures compared to that of underground structures in non-liquefied soil, which in turn increases the internal forces and deformation of the structure.

This study investigated the seismic response of underground structures in three typical soil profiles to highlight the significant influence of layered liquefiable ground. Further studies should be carried out to investigate more comprehensively the influence of factors including the position and thickness of the liquefiable layer, and the characteristics of the embedded structure.

References

[1] Samata S, Ohuchi H, Matsuda T. A study of the damage of subway structures during the 1995 Hanshin-Awaji earthquake. Cem Concr Compos 1997;19(3):223–39.

[2] Uenishi K, Sakurai S. Characteristic of the vertical seismic waves associated with the 1995 Hyogo-ken Nanbu (Kobe), Japan earthquake estimated from the failure of the Daikai Underground Station. Earthq Eng Struct Dyn 2000;29(6):813–22.

[3] Tokimatsu K, Tamura S, Suzuki H, Katsumata K. Building damage associated with geotechnical problems in the 2011 Tohoku Pacific Earthquake. Soils Found 2012;52(5):956–74.

[4] Yasuda S, Harada K, Ishikawa K, Kanemaru Y. Characteristics of liquefaction in Tokyo Bay area by the 2011 Great East Japan earthquake. Soils Found 2012;52(5):793–810.

[5] Yamaguchi A, Mori T, Kazama M, Yoshida N. Liquefaction in Tohoku district during the 2011 off the Pacific Coast of Tohoku Earthquake. Soils Found 2012;52(5):811–29.

[6] Yasuda S, Nagase H, Itafuji S, Sawada H, Mine K. A study on the mechanism of the floatation of buried pipes due to liquefaction. WIT Trans Built Environ 1995:14.

[7] Koseki J, Matsuo O, Koga Y. Uplift behavior of underground structures caused by liquefaction of surrounding soil during earthquake. Soils Found 1997;37(1):97–108.

[8] Orense RP, Morimoto I, Yamamoto Y, Yumiyama T, Yamamoto H, Sugawara K. Study on wall-type gravel drains as liquefaction countermeasure for underground structures. Soil Dyn Earthq Eng 2003;23(1):19–39.

[9] Tamari Y, Towhata I. Seismic soil-structure interaction of cross sections of flexible underground structures subjected to soil liquefaction. Soils Found 2003;43(2):69–87.

[10] Adalier K, Abdoun T, Dobry R, Phillips R, Yang D, Naesgaard E. Centrifuge modelling for seismic retrofit design of an immersed tube tunnel. Int J Phys Model Geotech 2003;3(2):23–35.

[11] Ling HI, Mohri Y, Kawabata T, Liu H, Burke C, Sun L. Centrifugal modeling of seismic behavior of large-diameter pipe in liquefiable soil. J Geotech Geoenviron Eng 2003;129(12):1092–101.

[12] Sasaki T, Tamura K. Prediction of liquefaction-induced uplift displacement of underground structures, In: Proceedings of the 36th Joint Meeting US-Japan Panel on Wind and Seismic Effects 2004; pp. 191–198.

[13] Kutter BL, Chou JC, Travasarou T. Centrifuge testing of the seismic performance of a submerged cut-and-cover tunnel in liquefiable soil. Geotech Earthq Eng Soil Dyn IV 2008:1–29.

[14] Chian SC, Madabhushi SPG. Effect of buried depth and diameter on uplift of underground structures in liquefied soils. Soil Dyn Earthq Eng 2012;41:181–90.

[15] Lee CJ, Wei YC, Chuang WY, Hung WY, Wu WL, Ho TY. Uplift mechanism of rectangular tunnel in liquefied soils. Geotechnical Hazards from Large Earthquakes and Heavy Rainfalls. Japan: Springer; 2017. p. 61–74.

[16] Chen G, Wang Z, Zuo X, Du X, Gao H. Shaking table test on the seismic failure characteristics of a subway station structure on liquefiable ground. Earthq Eng Struct Dyn 2013;42(10):1489–507.

[17] Zhuang H, Chen G, Hu Z, Qi C. Influence of soil liquefaction on the seismic response of a subway station in model tests. Bull Eng Geol Environ 2016;75(3):1169–82.

[18] Zhao D. Experimental study and numerical simulation on seismic response of urban underground subway structures. Civil Engineering. Beijing: Tsinghua University; 2013. [in Chinese].

[19] Yang D, Naesgaard E, Byrne PM, Adalier K, Abdoun T. Numerical model verification and calibration of George Massey Tunnel using centrifuge models. Can Geotech J 2004;41(5):921–42.

[20] Liu H, Song E. Seismic response of large underground structures in liquefiable soils subjected to horizontal and vertical earthquake excitations. Comput Geotech 2005;32(4):223–44.

[21] Azadi M, Hosseini SMMM. Analyses of the effect of seismic behavior of shallow tunnels in liquefiable grounds. Tunn Undergr Space Technol 2010;25(5):543–52.

[22] Saeedzadeh R, Hataf N. Uplift response of buried pipelines in saturated sand deposit under earthquake loading. Soil Dyn Earthq Eng 2011;31(10):1378–84.

[23] Chen R, Yao Y, Wang R, Zhang JM. Three-dimensional finite element analysis of underground structures' dynamic response in liquefiable soil. Adv Soil Dyn Found Eng 2014:572–8.

[24] Madabhushi SSC, Madabhushi SPG. Finite element analysis of floatation of rectangular tunnels following earthquake induced liquefaction. Indian Geotech J 2015;45(3):233–42.

[25] Zhuang H, Hu Z, Wang X, Chen G. Seismic responses of a large underground structure in liquefied soils by FEM numerical modelling. Bull Earthq Eng 2015;13(12):3645–68.

[26] Bao X, Xia Z, Ye G, Fu Y, Su D. Numerical analysis on the seismic behavior of a large metro subway tunnel in liquefiable ground. Tunn Undergr Space Technol 2017;66:91–106.

[27] Wang SP, Yan GX. Analysis on earthquake caused ground liquefying in shield driven tunnel section from Xufuxiang station to Nanjing station. Mod Tunn Technol 2001;4:19–23. [in Chinese].

[28] Hashash YMA, Hook JJ, Schmidt B, Yao JIC. Seismic design and analysis of underground structures. Tunn Undergr Space Technol 2001;16(4):247–93.

[29] Hashash YMA, Karina K, Koutsoftas D, O'Riordan N. Seismic design considerations for underground box structures In: Proceedings of the Earth Retention Conference 3; pp. 620–637; 2010.

[30] Zienkiewicz OC, Mroz Z. Generalized plasticity formulation and applications to geomechanics. Mech Eng Mater 1984;44(3):655–80.

[31] Elgamal A, Yang Z, Parra E. Computational modeling of cyclic mobility and post-liquefaction site response. Soil Dyn Earthq Eng 2002;22(4):259–71.

[32] Dafalias YF, Manzari MT. Simple plasticity sand model accounting for fabric change effects. J Eng Mech 2004;130(6):622–34.

[33] Dafalias YF, Taiebat M. SANISAND-Z: zero elastic range sand plasticity model. Geotechnique 2016;66(12):999–1013.

[34] Zhang JM, Wang G. Large post-liquefaction deformation of sand, part I: physical mechanism, constitutive description and numerical algorithm. ActaGeotechnica 2012;7(2):69–113.

[35] Wang R, Zhang JM, Wang G. A unified plasticity model for large post-liquefaction shear deformation of sand. Comput Geotech 2014;59:54–66.

[36] McKenna F, Fenves GL. OpenSees manual, PEER Center. ⟨http://OpenSees.berkeley.edu⟩.

[37] Zhang C, Luo Y, Bishir S. Research on the foundation using capability and zoning map in Nanjing. Hydrogeol Eng Geol 1999;26(1):13–6. [in Chinese].

[38] Mejia LH, Dawson EM. Earthquake deconvolution for FLAC. In: Proceedings of the 4th International FLAC Symposium on Numerical Modeling in Geomechanics., Minneapolis, Minn. 2006. p. 04-10.

[39] Wang R, Fu P, Zhang JM. Finite element model for piles in liquefiable ground. Comput Geotech 2016;72:1–14.

[40] PRC National Standard. Code for design of concrete structures (GB 50010-2010), The Ministry of Housing and Urban-Rural Construction of the People's Republic of China. Beijing, China: China Architecture & Building Press; 2010. [in Chinese].

[41] Zienkiewicz OC, Chan AHC, Pastor M, Schrefler BA. Computational Geomechanics. Chichester: Wiley; 1999.

[42] Yang Z, Lu J, Elgamal A. OpenSees Soil Models and Solid-Fluid Fully Coupled Elements. User's Manual. Ver, 1. 2008.

[43] Wang R. Single piles in liquefiable ground: seismic response and numerical analysis methods. Springer; 2016.

[44] Dafalias YF, Popov EP. A model of nonlinearly hardening materials for complex loading. Acta Mech 1975;21(3):173–92.

[45] Wang R, Liu X, Zhang JM. Numerical analysis of the seismic inertial and kinematic effects on pile bending moment in liquefiable soils. Acta Geotech 2017;12(4):773–91.

[46] Clough GW, Duncan JM. Finite element analyses of retaining wall behavior. J Soil Mech Found Div 1971.

[47] Tamate S, Towhata I. Numerical simulation of ground flow caused by seismic liquefaction. Soil Dyn Earthq Eng 1999;18(7):473–85.

[48] Dunn SL, Vun PL, Chan AHC, et al. Numerical modeling of wave-induced liquefaction around pipelines. J Waterw, Port, Coast, Ocean Eng 2006;132(4):276–88.

[49] Namikawa T, Koseki J, Suzuki Y. Finite element analysis of lattice-shaped ground improvement by cement-mixing for liquefaction mitigation. Soils Found 2007;47(3):559–76.

[50] NEHRP. Selecting and scaling earthquake ground motions for performing response-history analyses. Technical Report Prepared for the National Institute of Standards and Technology NIST GCR 11-917-15. National Earthquake Hazards Reduction Program (NEHRP) Consultants Joint Venture, Redwood City, Calif; 2011.

[51] Taiebat M, Amirzehni E, Finn WDL. Seismic design of basement walls: evaluation of current practice in British Columbia. Can Geotech J 2014;51(9):1004–20.

[52] PEER. Pacific Earthquake Engineering Research Center strong motion database. [Accessed on 6 November 2016.]; 2016.

[53] PRC National Standard. Code for seismic design of buildings (GB 50011-2010), The Ministry of Housing and Urban-Rural Construction of the People's Republic of China. Beijing, China: China Architecture & Building Press; 2010. [in Chinese].

[54] Seismosoft. SeismoSignal. Version 4.1.2; 2009b.

[55] Code P. Eurocode 8: Design of structures for earthquake resistance-part 1: general rules, seismic actions and rules for buildings; 2005.

[56] ASCE. ASCE/SEI7-05, Minimum design loads for buildings and other structures; 2005.